Stray-light analyses of the METIS Coronagraph on Solar Orbiter

S. Fineschi, INAF-Astrophysical Observatory of Torino, Italy – fineschi@oato.inaf.it
P. Sandri, CGS, Italy - psandri@cgspace.it
F. Landini, INAF-Astrophysical Observatory of Arcetri, Italy – flandini@arcetri.astro.it
M. Romoli, Florence University, Italy - marco.romoli@unifi.it
V. DaDeppo, CNR-IFN, Padova, Italy - vania.dadeppo@ifn.cnr.it
F. Frassetto CNR-IFN, Padova, Italy - frassetto@dei.unipd.it
E. Verroi, CISAS, Padua University – verroi@dei.unipd.it
G. Naletto, Padua University, Italy - naletto@dei.unipd.it
D. Morea, CGS, Italy – dmorea@cgspace.it
E. Antonucci, INAF-Astrophysical Observatory of Torino, Italy – antonucci@oato.inaf.it
D. Spadaro INAF – Astronomical Observatory of Catania dspadaro@oact.inaf.it
V. Andretta INAF - Astronomical Observatory of Capodimonte andretta@oacn.inaf.it

ABSTRACT

The METIS coronagraph on board the Solar Orbiter mission will have the unique opportunity of observing the solar outer atmosphere as close to the Sun as 0.28 A.U., and from up to 35° out-of-ecliptic. The telescope design of the METIS coronagraph includes two optical paths: i) broad-band imaging of the full corona in linearly polarized visible-light (VL: 580-640 nm), ii) narrow-band imaging of the full corona in the ultraviolet (UV) Lyman α (121.6 nm).

This paper describes the stray-light analyses performed on the UV and VL channels of the METIS Telescope with the non-sequential modality of Zemax OpticStudio. A detailed opto-mechanical model of the METIS Telescope is simulated by placing the CAD parts of all the sub-assemblies at the nominal position. Each surface, mechanical and optical, is provided with a modelled coating and BSDF reproducing the optical and the diffusing properties.

The geometric model allows for the verification of the correct functioning of the blocking elements inside the telescope and for an evaluation of the stray-light level due to surface roughness. The diffraction off the inner edge of the IEO on the plane of the IO is modelled separately from the contributor of the surface micro-roughness. The contributors due to particle contamination and cosmetic defects are also analysed. The results obtained are merged together and compared to the requirements of stray-light. The results of this analysis together with those from two different analyses based on a Montecarlo ray-trace and a semi-analytical model are consistent with each other and indicate that the METIS design meets the stray-light level requirements

Keyword list
METIS Telescope, stray-light, roughness, diffraction, contamination, cosmetics.

1. METIS TELESCOPE

METIS is one of the six remote sensing instruments for the Solar Orbiter mission and it is the result of a collaboration among members of an international scientific consortium Ref.[1] and Ref.[2].

METIS is an inverted-occulted coronagraph for simultaneous broad-band imaging of the solar corona in the visible light (VL), 580 nm - 640 nm, and narrow-band (FWHM = 10 nm) imaging in the ultraviolet (UV) wavelength of 121.6 nm.

2. FIGURES OF MERIT FOR THE STRAY-LIGHT

Since the coronal light is enormously fainter than the photospheric one, a very demanding suppression is needed for the internal stray light. The required ratio between the stray light irradiance B_{stray} (photons cm^{-2}s^{-1}) measured on the Telescope focal plane to the solar disk mean irradiance B_{sun} for the VL channel is $\mathrm{B_{stray}/B_{sun}} < 10^{-9}$ and for the UV channel is $\mathrm{B_{stray}/B_{sun}} < 10^{-7}$.

Solar Physics and Space Weather Instrumentation VI, edited by Silvano Fineschi,
Judy Fennelly, Proc. of SPIE Vol. 9604, 96040K · © 2015 SPIE
CCC code: 0277-786X/15/$18 · doi: 10.1117/12.2203629

3. MODEL OF THE TELESCOPE

3.1 Opto-mechanical model

A detailed opto-mechanical model of the Telescope is simulated by using the non-sequential modality of Zemax, which allows for importing the geometric models, e.g. in the form of step files, of the sub-assemblies and by placing them at the nominal position along the optical axis (Ref.[1], Ref.[2] and Ref.[3]).

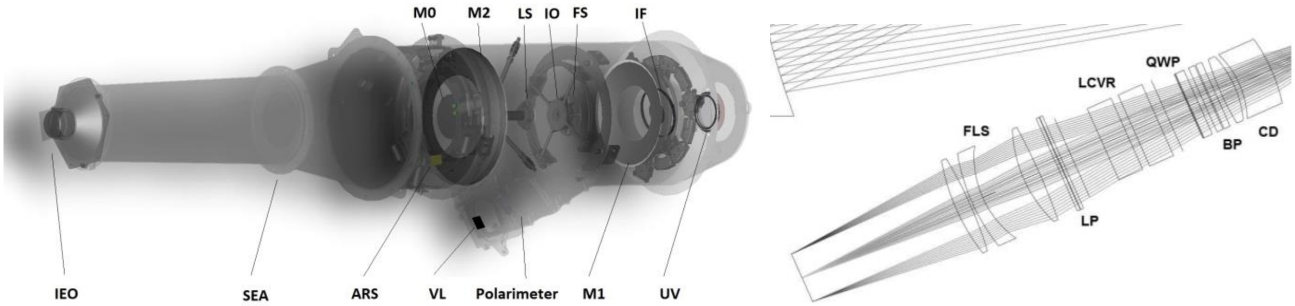

Figure 3-1. Left: layout of the Telescope. Right: Sectional view of the Polarimeter for the VL channel.

Left panel of Figure 3-1 shows the nominal, that is without manufacturing and alignment errors, opto-mechanical layout of the Telescope. Moving from left to right along the optical axis of the Telescope it can be seen the Inverted External Occulter (IEO), the baffle Shield Entrance Aperture (SEA), the mirror M0 with the Lyot Stop (LS), the mirror M2 of the Gregorian Telescope, the un-blackened alignment reference surface (ARS) on the rear side of the mirror M2 (there is an ARS on the rear side of M1 also for alignment purposes), the Internal Occulter (IO), the Field Stop (FS), the mirror M1 of the Gregorian Telescope, the Interference Filter (IF) tilted at 12° wrt the optical axis and the sensitive area of the UV detector. The UV detector presents a magnesium fluoride protective window with thickness 4mm. The IF with its beam splitter coating identifies a second path: the VL channel with the optical axis tilted at 24° wrt the optical axis of the UV channel. The imaging lens is represented by the Polarimeter working at finite conjugate between the intermediate focal plane of the Telescope and the sensitive area of the VL channel.

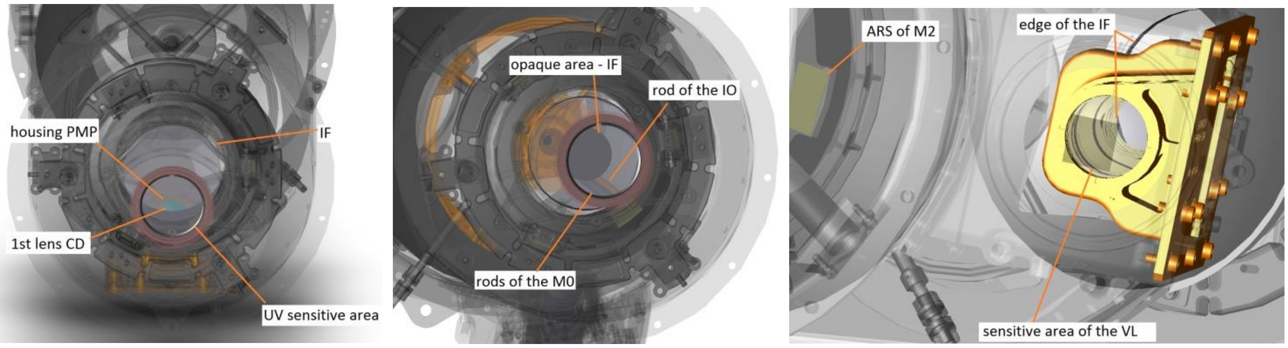

Figure 3-2. Insight view of the Telescope from the UV sensitive area (left and center) and from the VL sensitive area (right).

Right panel of Figure 3-1 shows the optical elements of the Polarimeter with the Collimating Doublet (CD) which is an air spaced doublet with diameter 27mm, the Band Pass (BP) filter made of two substrates in Schott rad-hard BK7G18, the Quarter Wave Plate (QWP), the Polarimetric group based on Liquid Crystal Variable Retarders (LCVR), the Linear Polarizer (LP) and the Focussing Lens System (FLS) made of an air-spaced triplet with outer diameter 39mm. The nominal back focal length of the Polarimeter is 65mm. The Quarter Wave Plate (QWP) is made of a quartz crystalline plate (278micron thickness) cemented onto a MgF_2 crystalline plate (226micron thickness) cemented on a supporting lamina of fused silica with thickness 3,5mm. The LP is a layer of prolate sphere embedded into a soda lime substrate (200microns approximately) cemented between two Schott radiation hardened K5G20 laminae, each one with thickness 1,2mm. the nanoparticles show strong plasmon absorption resulting in a polarization of the beam.

A three-dimensional opto-mechanical model of the Telescope allows for a deep insight view of the instrument. Figure 3-2 reports a view of the inner parts of the Telescope from the sensitive area of the UV and VL detector. Left panel shows the first lens of the Collimating Doublet and the top of the housing of the Polarimeter seen from the UV sensitive area; central panel shows the four rods of the IO-Assembly and M0-Assembly seen from the UV sensitive area and right panel shows the Polarimeter seen from the sensitive area of the VL detector.
As the results of the stray-light simulations and thus the compliance to the functional requirements mainly depend on how the physical properties of the objects hit by the optical rays are reproduced, the maximum effort has been used in modelling all the surfaces reproducing their reflecting, transmitting, absorbing (in some cases) and diffusing properties.

3.2 Model of the coatings

The functional coatings deposited on the opto-mechanical elements are simulated in Zemax. Each opto-mechanical surface is assigned with a property of reflection, transmission and in some cases absorption as a function of the wavelength replicating the coatings deposited on the optical surfaces. The models of the coatings are reported in Figure 3-3. From top to bottom row:
In the first row:

- Left: the model of the metallic coating (aluminium with a protective layer of magnesium fluoride) for the mirrors M1 and M2 of the Gregorian telescope in the spectral range [120, 1000]nm;
- Centre: the anti-reflection coating for the lenses of the CD and FLS, for the QWP and LP in the spectral range [500, 700]nm;
- Right: the reflection and transmission of the IF for AOI of 12degrees in the spectral range [120, 720] nm. The central area of the IF with a diameter 37mm has been simulated with an absorbing coating.

In the second row:

- Left: the transmission of the Band Pass (BP) filter in the spectral range [500, 700]nm;
- Centre: the transmission of the Linear Polarizer (LP) from Codixx in the spectral range [500, 700]nm;
- Right: the reflectivity of the Acktar Black Magic in the spectral range [120, 700]nm. The Black Magic is applied on all the metallic parts and on the ground surfaces of the mirrors. The inner wall of the carbon fibre tube connecting M1 to M2 is covered with a Metal Velvet foil having similar properties to the Black Magic (R<1%, TIS 3%). The housing of the PMP is coated with Astro Black from Metal Estalki (R5%, TIS 14%). The only un-blackened areas in the telescope are the ARS (12x20mm^2) on the rear side of M1, the ARS (28x15mm^2) on the rear side of M2 needed for alignment purposes, the outer ground edge of the IF and the interfaces on the rear side of the mirrors dedicated to the cementing with structural frames.
-

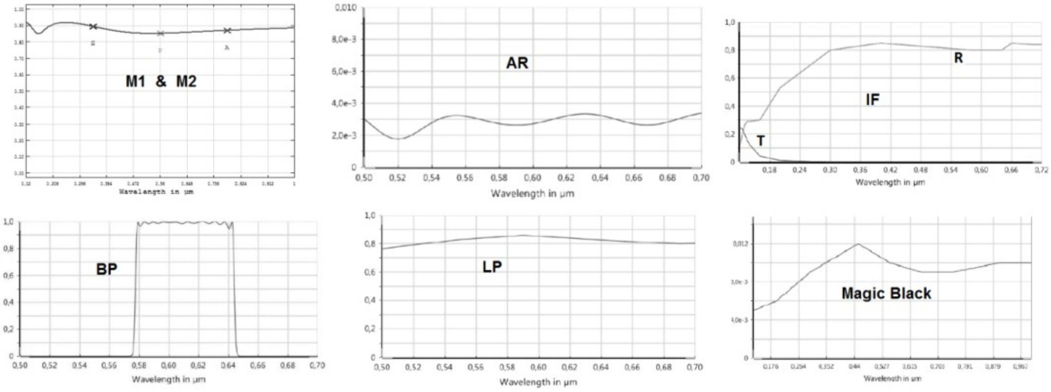

Figure 3-3. Transmission/Reflection curves of the modelled coatings.

3.3 Model of the detectors

The model of the Telescope includes also the UV and VL detectors. The sensitive area of the VL is modelled with a reflectivity given by the complementary to the Quantum Efficiency (QE). The simulated QE the reflectivity of the VL detector are respectively reported in left and right panel of Figure 3-4. The AR coating of the sensitive area is already included in the curve of QE.

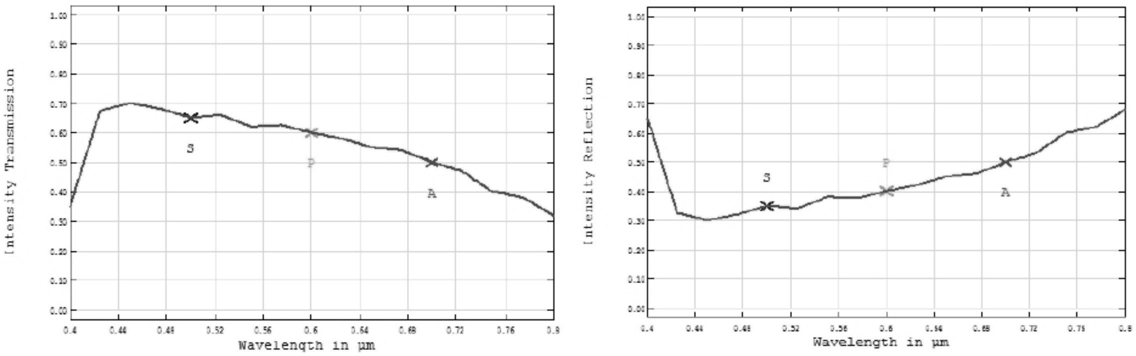

Figure 3-4. Simulated QE (left) and reflectivity (right) of the sensitive area of the VLDA.

The UV Intensifier has been modelled according to technical data from MPS with an uncoated MgF_2 protective window with thickness 4mm, the multi-pore surface coated with KBr and the mechanical parts made in white ceramic and uncoated stainless steel. The reflectivity of the uncoated stainless steel has been assumed 1% for the wavelength of 121nm. The remaining part of radiation is assumed to be completely absorbed. The same assumption has been made for the white ceramic parts of the UV intensifier. The sensitive area of the UV detector is modelled with a reflectivity of approximately 1% corresponding to the reflectivity of a multi-pore surface coated with KBr.

3.4 Simulation of roughness of the optical and of the mechanical surfaces

All the mechanical parts of the model of Telescope and of the Sub-Assembles (e.g. is the IEO, the boom, the baffle SEA, the conical junction, the carbon fibre tube connecting mirror M1 to mirror M2, the Lyot Stop, the rods, the mechanical parts of the M1 sub-assembly and of the M2 sub-assembly, the IO sub-assembly, the IF sub-assembly, the ground surfaces of the mirrors) have been provided with a Lambertian scattering with a fraction of scattered rays of 0,03. This assumption relies on the results of the measurement performed by the MST reported in Figure 3-5. The scatter fraction for the housing of the PMP, coated with Astro Black Metal Estalki, is considered 14% (value from the data sheet).
Figure 3-5 reports (by courtesy of the MST) the measured BRDF for two different angle of incidence (AOI 5° and 70°) on samples coated with different black coatings. Each plot reports the BRDF evaluated as a function of the observing angle (0 degree corresponds to the direction normal to the sample). The left (right) panels of Figure 3-5 report the measurement for a scan along (perpendicular to) the plane of incidence. The curve of Acktar Black Magic is the lowest.

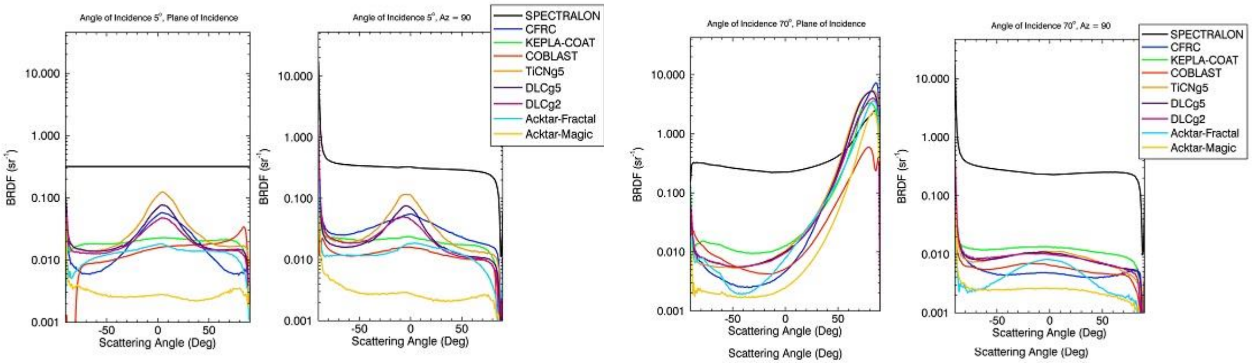

Figure 3-5. BRDF for AOI 5°(left) and 70° (right) (courtesy of MST).

The surface micro-roughness of the optical surfaces is simulated with the ABg analytical model. The parameters A, B and g define the overall amplitude, the roll-off angle and the log-log shape of the scattering BSDF respectively (Ref.[4]). Table 3-1 reports the surface micro-roughness σ_{rel} in the spatial frequency band limit Ref.[5], the value of the parameters and the TIS evaluated with Zemax. The values of A, B and g inserted in Zemax OpticStudio for a specific wavelength are scaled by Zemax OpticStudio for different working wavelengths Ref.[6].

Item	σ_{rel} *roughness*	*Parameters of the ABg model*	*λ (nm)*	*TIS*
Mirror M1	0,3nm, f<0,1[1/µm]	A = 3,82E-5, B = 1,04E-8, g = 2	121,6	0,0022059
Mirror M2	2nm, f<0,1[1/µm]	A = 0,0017, B = 1,04E-8, g = 2	121,6	0,0981700
Mirror M0	0,3nm, f>0,1[1/µm]	A = 3,82E-5, B = 2,35E-13, g = 2	121,6	0,0033160
Align. Ref. Surface	2nm	A = 0,0017, B = 1,04E-8, g = 2	121,6	0,0981700
window of MCP	3nm	A = 0,000349, B = 1,04E-8, g = 2	121,6	0,0201537
Interferential Filter	1nm	A = 3,88E-5, B = 1,04E-8, g = 2	121,6	0,0022406
Lenses in SF6G05	2nm	A = 1,1E-5, B = 9,4E-11, g = 2	610	0,0007979
Lenses in BK7G18	2nm	A = 4,55E-6, B = 9,4E-11, g = 2	610	0,0003300
Items in fused silica	2nm	A = 3,54E-6, B = 9,4E-11, g = 2	610	0,0002568

Table 3-1. values of the parameters of the ABg model for the surface roughness.

4. STRAY-LIGHT ANALYSIS

The analysis of stray-light is performed by using the geometric model of the Telescope and then adding the contributors due to the diffraction off the edges of the IEO, to the particulate contamination and to the cosmetic defects.
We start from the geometric model of the Telescope built as described in previous Sections with a source placed externally of the IEO simulating the Sun. This approach allows for:

A. A verification that the solar disk is efficiently blocked by the rejection mirror M0, the Field Stop, the Internal Occulter and the Lyot Stop. For this purpose we consider the Sun in the most critical position for the generation of diffuse light at the distance of 0.28AU from the instrument. The Sun is simulated with a *source two angle* with an angular extension of ±0,954degrees in X and Y directions (Z s the optical axis).

B. An evaluation of the level of noise due to the surface micro-roughness on the simulated images of the corona. For this purpose we consider a source with an angular extension equal to the instrumental FoV, ±2,9degrees.

Then we focus attention on the diffraction due to the finite aperture of the mirror M1. To keep separate the contributors due to micro-roughness from that of the diffraction we simulated:

C. The illumination of the IO due to the diffraction from the M1 vignetting with a simplified model of the Telescope consisting only of: the mirror M0, the rear circular aperture of the mirror M2, the mirror M1, the FS and the IO. In this model the mirror M1 and the mechanical items are simulated as perfect surfaces without micro-roughness.

Then we introduce the contributor due to particulate contamination and to cosmetic defects. Each contributor is analysed with a dedicated simulation, thus keeping separated their effects. The results are merged together and compared to the requirements of stray-light level.

4.1 Stray-light level due to surface micro-roughness with the Geometric model of the Telescope

4.1.1 Verification of the correct functioning of the blocking elements with the Sun at the perihelion

As per point A of Sect. 4 we compute the level of spurious light on the UV and VL detectors due to the illumination coming from the solar disk at the minimum perihelion. The analysis is performed with the following set-up:

- Sun modelled with the "*source two angle"* placed 1mm out of the external edge of the IEO, with circular shape, angular extension of ± 0,954° and a normalized power equal to 1 Watt over the spectral range,
- FoV = ± 0,954° corresponding to the angular extension of the Sun at the minimum perihelion (0,28AU);
- Sun pointing, that is considering tilt X, Y= 0 (Z is the optical axis in Zemax); Wavelength range [0.12; 0.8]µm;
- Nominal design (nor alignment neither integration errors) of the Telescope;
- The maximum number of analysis rays (1E7) is limited by the duration of the simulation;
- minimum relative ray Intensity (threshold value, Ref.[3]) = 1E-15W.

The solar disk should be completely blocked by the mirror M0. In fact the radial aperture of M0 satisfies the relation:

$$R_{M0} > R_{IEO} + L\tan(0{,}954°) = 33{,}32mm$$

where $R_{M0} = 35{,}5$mm the radial aperture of the mirror M0, R_{IEO}=20mm the external radial aperture of the IEO and L= 800mm the distance from the IEO to the vertex of the spherical concave mirror M0. The results are in Table 4-1.

	Analysis rays	*UV image plane*		*VL image plane*	
		No. of collected rays	*Total power (Watt)*	*No. of collected rays*	*Total power (Watt)*
1st run	2E6	2857	9,0e-15	337	5,7E-15
2nd run	1E7	14023	1,48e-14	1706	3,32E-15

Table 4-1. Results of stray-light analysis with the Sun disk at the minimum perihelion.

Figure 4-1 reports in logarithmic scale the rays collected on the virtual detectors placed at the UV and VL image planes. The dimensions of the virtual detectors are (42,3 × 42,3)mm^2 for the UV channel and (20,4 × 20,4) mm^2 for the VL channel.

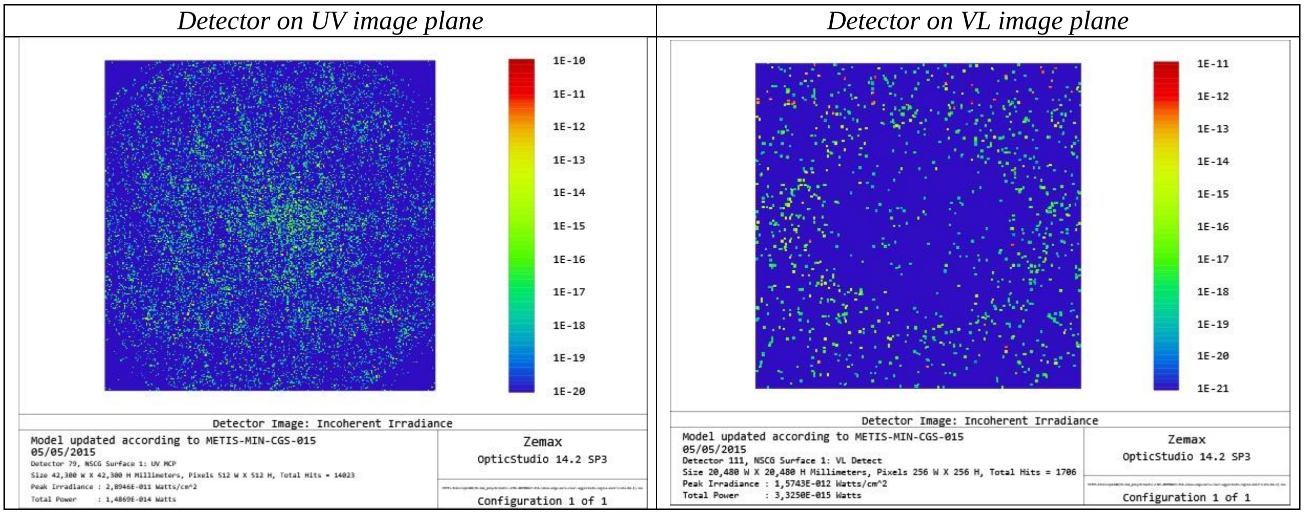

Figure 4-1. Simulated images of the UV and VL virtual detectors for FoV±0,954° (log scale).

The ratio of the intensities of the spurious rays reaching the detectors to the input power, for a source with an angular extension equal to the solar disk placed at the minimum perihelion, results:

$$\left.\frac{I_{spurious-rays}}{I_{input}}\right|_{UV\ channel} \approx 1 \cdot 10^{-14} \qquad \left.\frac{I_{spurious-rays}}{I_{input}}\right|_{VL\ channel} \approx 3 \cdot 10^{-15}$$

This allows to conclude that the blocking elements efficiently stop the Sun disk.

4.1.2 Stray-light due to surface micro-roughness with the instrumental FoV

To evaluate the contributor of stray-light due to surface micro-roughness (point B of Sect. 4) we perform a simulation with the following settings:

- "*source two angle"* placed 1mm out of the external edge of the IEO, with circular shape, angular extension of ± 2,9° and a normalized power equal to 1 Watt over the spectral range,
- Sun pointing, that is considering tilt X = tilt Y= 0 (Z is the optical axis in Zemax); spectral range [0.12; 0.8]µm;
- Nominal design of the Telescope, and edge of the Interference Filter un-blackened;
- Analysis rays = 1E6, minimum relative ray Intensity (threshold value, Ref.[3]) = 1E-15W.

The un-blackened edge of IF has no impact on the irradiances, though it receives 12% of total rays (power of 7,2E-8W).

The simulated images for the UV and VL detectors are reported in Figure 4-2 in logarithmic scale and for the mirror M1 and the IF in Figure 4-3 in linear scale. Figure 4-2 shows in red colour the imaged corona and in green colour the noise. Letters A and B adjacent to the simulated UV image identify a section respectively placed at Y=0 and at Y=5,5mm.

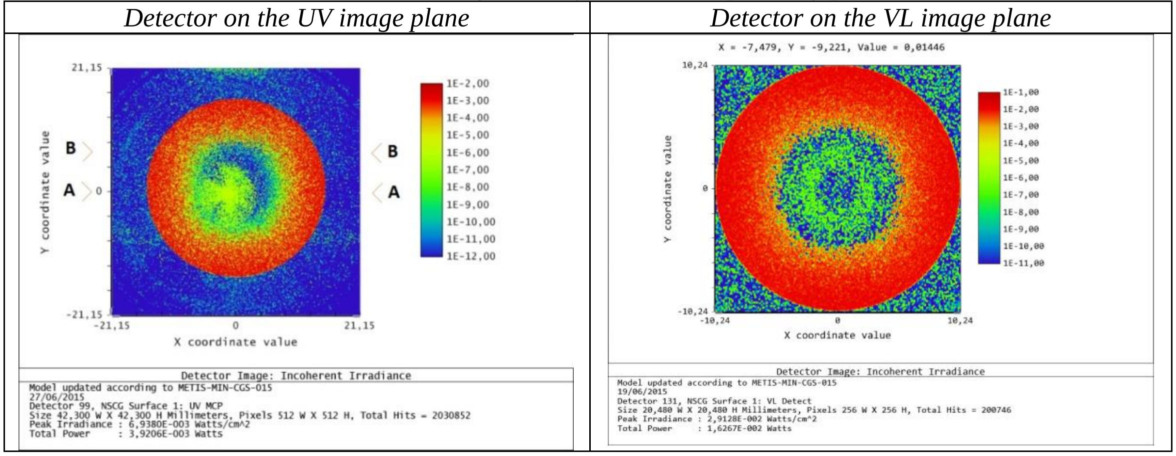

Detector on the UV image plane

Detector on the VL image plane

```
Detector Image: Incoherent Irradiance
Model updated according to METIS-MIN-CGS-015
27/06/2015
Detector 99, NSCG Surface 1: UV MCP
Size 42,300 W X 42,300 H Millimeters, Pixels 512 W X 512 H, Total Hits = 2030852
Peak Irradiance : 6,9380E-003 Watts/cm^2
Total Power     : 3,9206E-003 Watts
```

```
Detector Image: Incoherent Irradiance
Model updated according to METIS-MIN-CGS-015
19/06/2015
Detector 131, NSCG Surface 1: VL Detect
Size 20,480 W X 20,480 H Millimeters, Pixels 256 W X 256 H, Total Hits = 200746
Peak Irradiance : 2,9128E-002 Watts/cm^2
Total Power     : 1,6267E-002 Watts
```

Figure 4-2. Simulated images on the UV/VL (left/right) detectors in logarithmic scale.

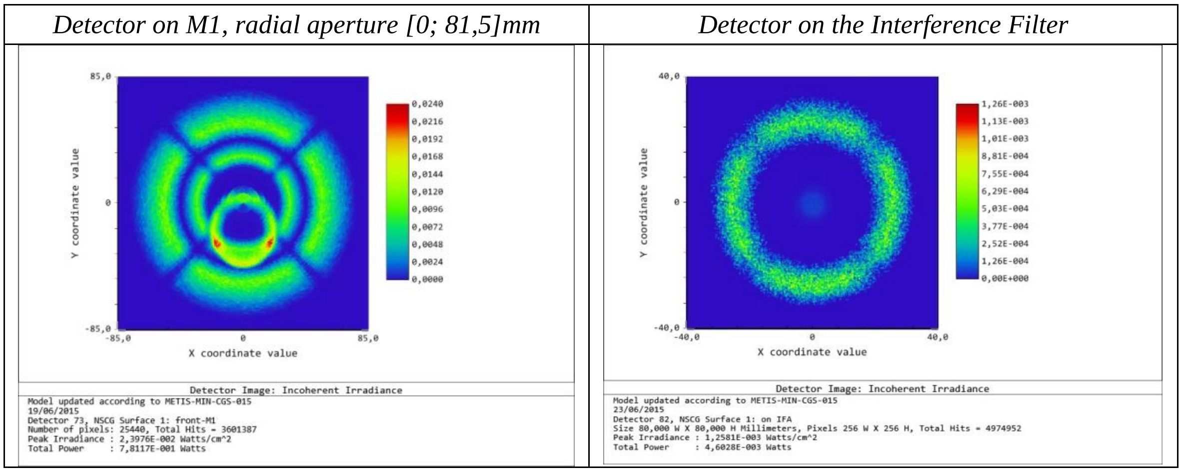

Detector on M1, radial aperture [0; 81,5]mm

Detector on the Interference Filter

```
Detector Image: Incoherent Irradiance
Model updated according to METIS-MIN-CGS-015
19/06/2015
Detector 73, NSCG Surface 1: front-M1
Number of pixels: 25440, Total Hits = 3601387
Peak Irradiance : 2,3976E-002 Watts/cm^2
Total Power     : 7,8117E-001 Watts
```

```
Detector Image: Incoherent Irradiance
Model updated according to METIS-MIN-CGS-015
23/06/2015
Detector 82, NSCG Surface 1: on IFA
Size 80,000 W X 80,000 H Millimeters, Pixels 256 W X 256 H, Total Hits = 4974952
Peak Irradiance : 1,2581E-003 Watts/cm^2
Total Power     : 4,6028E-003 Watts
```

Figure 4-3. Simulated images on mirror M1/Interference Filter (left/right) in linear scale.

In left panel of Figure 4-3 the outer illuminated green ring in M1 represents the sun corona, the central illuminated corona is due to the rays travelling from M2 toward the IF, the small decentred corona represents the rays reflected from the IF and travelling toward the first lens of the CD of the Polarimeter. Figure 4-4 reports the simulated irradiance profiles on the UV and VL image planes compared to the profiles obtained with no scattering (green dotted curves). For the UV channel two irradiance profiles are plotted, along the section AA/BB(solid/dashed curve) of Figure 4-2. For the VL channel the irradiance profile is along the horizontal central row.

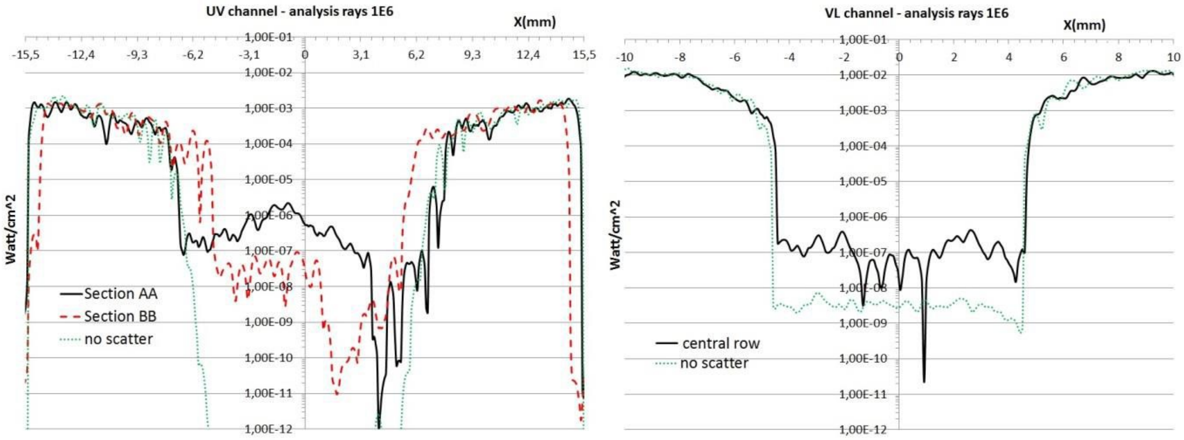

Figure 4-4. Simulated irradiance profile for the UV (left) and for the VL (right) detector in logarithmic scale.

The simulated irradiance profile of the imaged corona in the UV channel shows a higher noise wrt the profile of the VL channel. This is due to the modelled IF coating which has approximately a ratio 4:1 between the reflected and the transmitted rays (R≈80% in VL, T≈20% in UV) resulting in a lower statistics for the UV channel. Furthermore the irradiance profiles of the imaged corona show an increasing intensity as a function of the instrumental FoV reflecting the vignetting plot.

To evaluate the ratio B_{stray}/B_{corona} we assume that spurious rays are approximately uniformly distributed over the whole sensitive area of the detectors. This assumption is justified looking at the simulated irradiance on detectors (Figure 4-2) where, apart from a peak placed close to the centre of the UV detector, the noise is almost uniform. The average of the spurious irradiance in the UV channel is evaluated along the section B-B of Figure 4-2 which avoids the central peak. The peak is due to rays retro-reflected by the coated IF (T≈23%, R≈14% at wavelength of 121,6nm from Acton) toward the Polarimeter which in turn are retro-reflected by the first lens of the CD of the Polarimeter.

Table 4-2 reports in columns from left to right the analysis of the intensity profiles of Figure 4-4:

- the irradiance B_{stray} of spurious rays averaged in an interval selected in a central area of the detector limited by the inner radial aperture of the imaged corona;
- the irradiance B_{corona} averaged inside the imaged corona;
- the ratio B_{stray}/B_{corona}.

Item	*Averaged B_{stray} (Watt/cm^2) due to roughness*	*Averaged B_{corona} (Watt/cm^2)*	B_{stray}/B_{corona}
UVDA	2,29E-8 in [-4; 4]mm along sect. B-B	7,27E-4	3,16E-5
VLDA	1,32E-7 in [-4; 4]mm	7,17E-3	1,84E-5

Table 4-2. Simulated irradiances and ratio B_{stray}/B_{corona} due to surface micro-roughness.

The ratio B_{stray}/B_{corona} due to surface micro-roughness is $3{,}16 \cdot 10^{-5}$ for the UV channel and $1{,}84 \cdot 10^{-5}$ for the VL channel. Considering that the ratio B_{corona}/B_{Sun} is $\sim 5 \cdot 10^{-5}$ at the HI-Lyman alpha (121,6nm) and $\sim 1 \cdot 10^{-6}$ in the visible light (Ref.[7], Ref.[8]) it results:

$$\left.\frac{B_{stray}}{B_{sun}}\right|_{UV,roughness} \approx 1{,}6 \cdot 10^{-9} \quad \text{and} \quad \left.\frac{B_{stray}}{B_{sun}}\right|_{VL,roughness} \approx 1{,}84 \cdot 10^{-11}$$

4.1.3 Accuracy of the geometric model

The accuracy of the geometric model has been tested on a set of three simulations all performed with the same settings, with the model for the surface micro-roughness. The number of rays and the power collected on the UV and VL virtual detector are reported in Table 4-3. The maximum deviation from the mean value of the collected rays is 0,22% for UV channel and 0,67% for the VL channel.

Analysis rays 1E6 Input power 1W	*UV image plane*		*VL image plane*	
	No. of collected rays	*Collected power*	*No. of collected rays*	*Collected power*
1st run	2030852	3,9206E-3W	200746	1,6267E-2W
2nd run	2023750	3,9241E-3W	201701	1,6285E-2W
3rd run	2024770	3,9365E-3W	198667	1,6268E-2W

Table 4-3. Results of four different runs obtained with the geometric model.

4.2 Stray-light due to the diffraction from the M1 vignetting

4.2.1 Evaluation of the ratio B_{stray}/B_{M1}

We now evaluate (point C of Sect. 4) the illumination of the IO due to the diffraction off the IEO generated by the finite aperture, shaped as an annular corona, identified by the rear aperture of the mirror M2 (plane A of left panel of Figure 4-5) with diameter 120,4mm and by the mirror M0 (plane B of left panel of Figure 4-5) with diameter 71mm.

We use a simplified model consisting of: the rear aperture of mirror M2, the mirror M0, the mirror M1, the FS and the IO (right panel of Figure 4-5). In this model the mirror M1 is modelled as a perfect surface with no roughness. The object is placed at a height of 20,56mm corresponding to the radial aperture of the inner edge of the IEO.

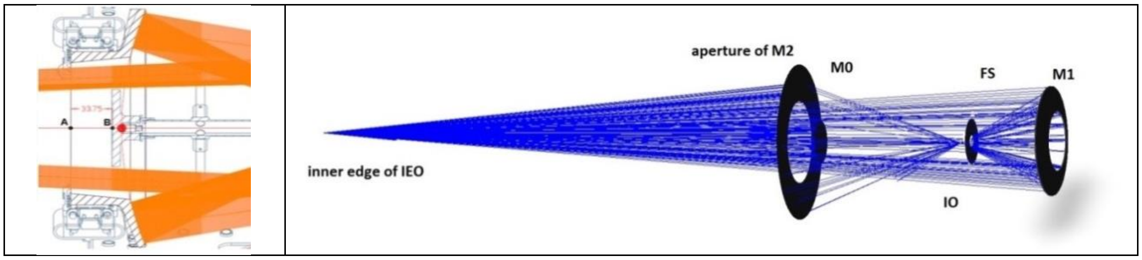

Figure 4-5. left: sectional view of M0 and M2 with ray-tracing for the FoV 2,9°. Right: model to include the diffraction.

The right panel of Figure 4-5 shows the ray tracing with the non-sequential modality of Zemax OpticStudio. The optical rays are partially vignetted by the mirror M0 and then are conjugated by mirror M1 on the IO. The FS blocks through vignetting a large amount of the rays travelling from mirror M1 toward the IO. The object height Y=20,56mm is conjugated by mirror M1 on IO at an image height of Y'= -2,775mm. The image is mainly aberrated by coma. The image is conjugated at a height larger than the radial aperture of the IO (the nominal value is 2,6mm) as reported in left panel of Figure 4-6. The virtual detector in left panel of Figure 4-6 has dimensions 5,6mm x 5,6mm. The orange circumference inside the blue virtual detector represents the radial aperture of the Internal Occulter with diameter 5,2mm. The central panel of the Figure 4-6 shows an enlarged view of a small area (0,15mm x 0,20mm) centred at Y= -2,70mm; the right panel of Figure 4-6 shows an enlarged view of a small area (0,20mm x 0,50mm) centred at Y= -2,60mm. This detector is divided into two halves separated by the radial aperture of IO. The bottom part is in shadow being blocked by the IO. The vertical Y coordinate in Figure 4-6 represents the distance from the optical axis.

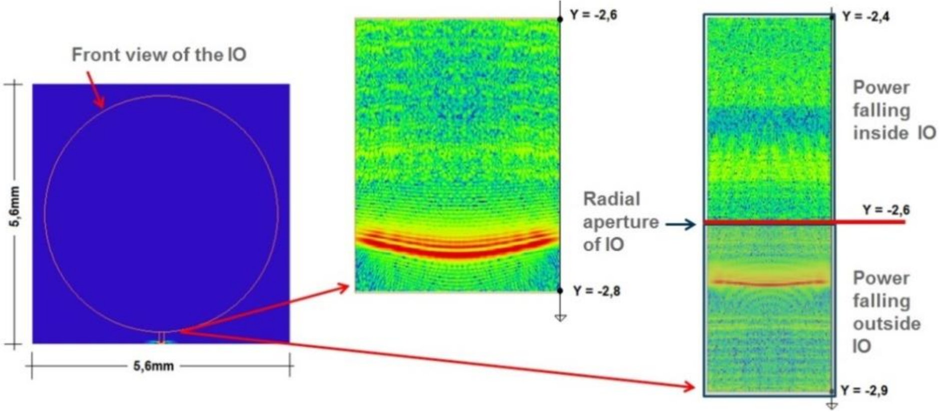

Figure 4-6. Diffraction at the IO with one single point object placed on the inner edge of the IEO. Left: image of the illuminated point object on the IO. Centre and right: enlarged views of a small area containing the image.

The non-sequential model has been verified for different wavelengths. The obtained results change for different wavelengths, as it should do because of the diffraction. Figure 4-7 shows the diffraction pattern on a small detector with dimensions 0,15mm x 0,20mm centred at Y= -2,70mm for three different wavelengths: 121nm (right), 580nm (centre) and 632nm (right). The image height is at Y = -2,77mm.

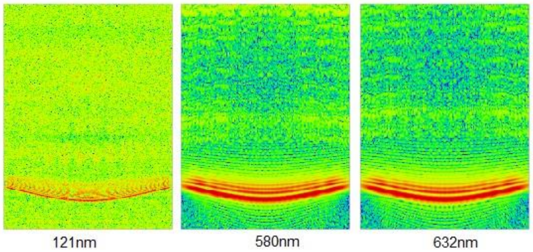

Figure 4-7. diffraction pattern on an area of 0,15x0,20mm^2 centered at Y=-2,7mm on the IO for wavelengths 121nm, 580nm and 632nm.

Left panel of Figure 4-8 shows the irradiance profile on the IO as a function of the distance from the optical axis in logarithmic scale. The irradiance profile shown in Figure 4-8 is obtained with one single illuminated object point placed on inner edge of the IEO. The vertical line of Figure 4-8 placed at Y=-2,6mm represents the edge of radial aperture of the IO. The vertical line at Y=0 represents the optical axis. The high intensity peak placed at Y =-2,77mm represents the image of the illuminated point object placed on the inner edge of the IEO. It is clear that high order diffraction rings illuminate the radial aperture of the IO.

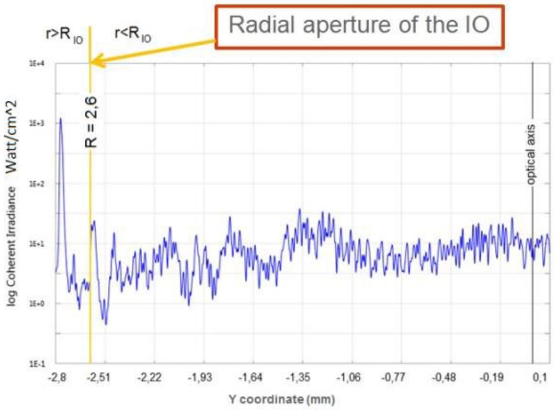

Figure 4-8. Irradiance profile as a function of the distance from the optical axis in log scale.

To evaluate the power that illuminates the IO due to diffraction we use two detector surfaces, both centred on the optical axis, the first with radial aperture 2,8mm and the second with a coronal aperture extending from 2,6mm to 2,8mm. Both detectors are divided in pixels with coherent data type. In fact in non-sequential modality, to account for diffraction effects, Zemax OpticStudio computes the real and imaginary parts of the electric field by using the intensity and phase of the ray referenced to the center of the pixel hit. The real and imaginary parts are then summed for many rays that strike the same pixel. The two detector surfaces are placed on the plane of the IO with a small (few microns) distance one from other along the optical axis as Zemax OpticStudio does not collect rays for overlapped detectors. Both detectors contain the image thus allowing Zemax OpticStudio to account for diffraction effects by summing the intensity (amplitude squared) for each pixel. The collected power at the IO due to one single illuminated object placed on the inner edge of the IEO results $8{,}3 \cdot 10^{-4} Watt$ for the spectral wavelength [580, 640]nm and $8{,}2 \cdot 10^{-4} Watt$ for the wavelength of 121,6nm. These values represent the average of 5 simulations each one performed with $1 \cdot 10^{6}$ analysis rays and the same settings. The ray tracing of right panel of Figure 4-5 has been performed with an object NA = 0,032 while the diffraction at the inner edge of IEO takes place with an angle of 2π rad. Therefore the collected power is scaled for the ratio of these solid angles. From these considerations B_{IO} at the IO due to diffraction, for UV and VL channel respectively, results:

$$B_{IO,VL} = B_{simulated,VL} \cdot \frac{\Omega_{model}}{\Omega_{total}} = 4{,}2 \cdot 10^{-7} Watt$$

$$B_{IO,UV} = B_{simulated,UV} \cdot \frac{\Omega_{model}}{\Omega_{total}} = 4{,}16 \cdot 10^{-7} Watt$$

being Ω_{model} the solid angle identified by the object numerical aperture used in the model.
Now the value of B_{IO} calculated at the IO should be propagated toward the focal planes considering the throughput of the VL and UV channels. Nevertheless in the requirement B_{stray}/B_{Sun}, the irradiance B_{sun} is intended measured on the focal plane and not at the entrance aperture. In other words B_{sun} represents the irradiance that should be measured at the focal plane in the absence of the occulters. Therefore also B_{sun} should be propagated toward the detectors thus the ratio of B_{UV} and B_{VL} to B_{sun} is equal to the ratio calculated with B_{IO}. Being from simulation $B_{M1} = 6{,}37 \cdot 10^{-1}$ Watt, the ratio of the power on detectors to the power on mirror M1 results:

$$\left.\frac{B_{stray}}{B_{M1}}\right|_{UV,diffr.} = \frac{4{,}2 \cdot 10^{-7}}{0{,}637} = 6{,}59 \cdot 10^{-7} \qquad \left.\frac{B_{stray}}{B_{M1}}\right|_{VL,diffr.} = \frac{4{,}16 \cdot 10^{-7}}{0{,}637} = 6{,}54 \cdot 10^{-7}$$

4.2.2 Measured ratio B_{M1}/B_{Sun}

The ratio of stray-light irradiance on mirror M1 to the solar disk irradiance has been measured in laboratory (Ref.[9]) with a breadboard of the Occulter Assembly with an accurate test campaign dedicated to evaluate the best optimization configuration for the IEO. Left panel of Figure 4-9 shows the design principle and the experimental set-up for the measurement. Right panel of Figure 4-9 shows the results of the measurements.

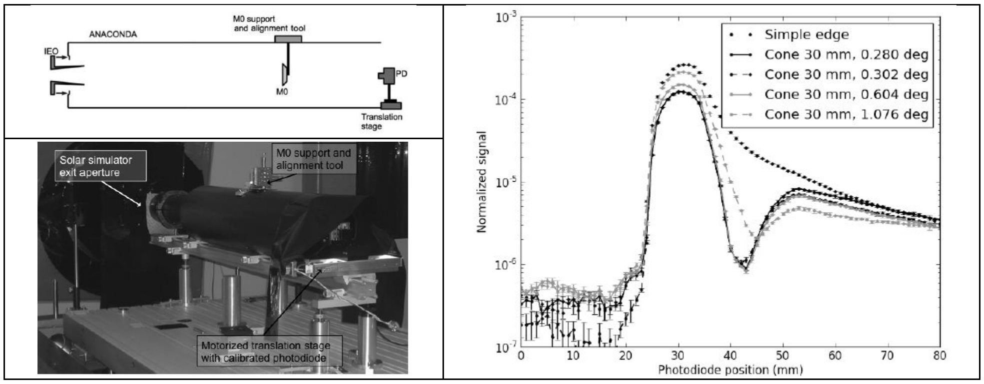

Figure 4-9. design principle (left top) and experimental set-up (left bottom). Measured ratio of stray-light irradiance on M1 to sun disk irradiance (right) (Ref.[9]).

The upper limit of the measured ratio of stray-light irradiance on mirror M1 to the solar disk irradiance results $B_{M1}/B_{Sun} \approx 1 \cdot 10^{-4}$. In the following we assume to have the same ratio also for the UV channel although it has been measured only for visible light. By putting together the evaluated B_{stray}/B_{M1} with the measured B_{M1}/B_{Sun} we obtain the contributor of the diffraction:

$$\left.\frac{B_{stray}}{B_{UV}}\right|_{diffr.} = 6{,}59 \cdot 10^{-11} \qquad \left.\frac{B_{stray}}{B_{VL}}\right|_{diffr.} = 6{,}54 \cdot 10^{-11}$$

4.3 Stray-light due to particulate contamination

The contributor to the stray-light due to particulate contamination is analysed with the model of Spyak and Wolfe Ref.[10]. The bidirectional scattering distribution function BSDF due to particulate contamination *f* as a function of the scattering angle is:

$$BSDF_S^{PAC} = f \cdot \left[\frac{0{,}15}{0{,}01 + \theta^{1{,}2}} + \frac{6 \cdot 10^{-5}}{10^{-7} + \theta^4}\right]$$

The dashed curve of Figure 4-10 obtained for a particle obscuration *f*=3,3ppm, the requirement for METIS at the beginning of life (BOL), is fitted with an analytical ABg model with parameters A=4E-7, B=2E-4 and g=2,2 obtaining the dot-dashed curve of Figure 4-10. These parameters are inserted in Zemax for the wavelength of 632,8nm, that is the wavelength of the measurement of Ref.[10]. The ABg scattering model is applied to the optical surfaces of the model of the Telescope for an analysis dedicated only to the contributor to stray-light due to particulate contamination. The simulation has been performed with 1E6 analysis rays. In Figure 4-10 we also plot the BSDF obtained with the model of Ref.[11] and Ref.[12].

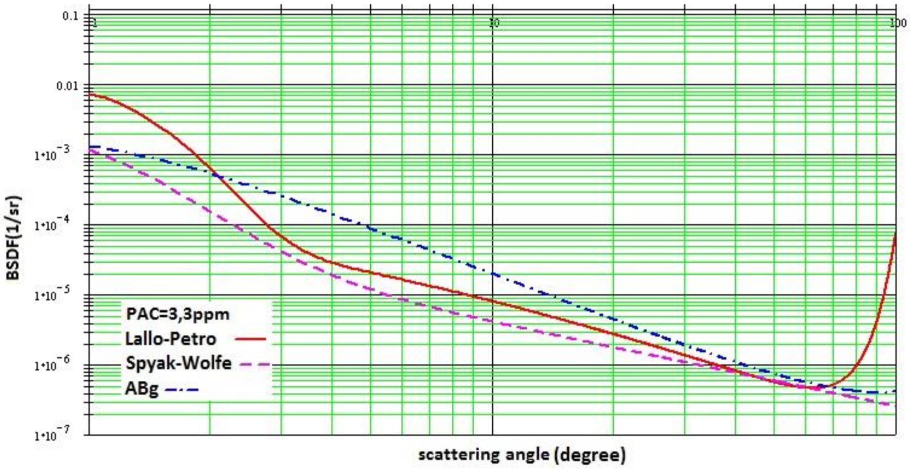

Figure 4-10. BSDF curve due to PAC 3,3ppm fitted with the ABg model (dot-dashed curve) for λ 632,8nm.

The results of the simulation are in Table 4-4. The value EOL is obtained by scaling the BOL value for 31ppm/3,3ppm.

Item	*Averaged B_{stray} (Watt/cm^2) due to PAC*	*Averaged B_{corona} (Watt/cm^2)*	B_{stray}/B_{corona} *BOL*	B_{stray}/B_{corona} *EOL*
UVDA	2,15E-8 in [-4; 4]mm	9,02E-4	2,39E-5	2,24E-4
VLDA	1,81E-7 in [-4; 4]mm	7,37E-3	2,47E-5	2,32E-4

Table 4-4. Simulated irradiance and ratio B_{stray}/B_{corona} due to particulate contamination.

The BOL ratio B_{stray}/B_{corona} due to particulate contamination is evaluated as in Sect. 4.1.2 and results $2{,}39 \cdot 10^{-5}$ for the UV channel and $2{,}47 \cdot 10^{-5}$ for the VL channel. Considering that the ratio B_{corona}/B_{Sun} is $\sim 5 \cdot 10^{-5}$ at the HI-Lyman alpha (121,6nm) and $\sim 1 \cdot 10^{-6}$ in the visible light (Ref.[7], Ref.[8]) it results respectively for BOL and EOL:

$$\left.\frac{B_{stray}}{B_{sun}}\right|_{UV,PAC-BOL} \approx 1{,}19 \cdot 10^{-9} \quad \text{and} \quad \left.\frac{B_{stray}}{B_{sun}}\right|_{VL,PAC-BOL} \approx 2{,}47 \cdot 10^{-11}$$

$$\left.\frac{B_{stray}}{B_{sun}}\right|_{UV,PAC-EOL} \approx 1{,}12 \cdot 10^{-8} \quad \text{and} \quad \left.\frac{B_{stray}}{B_{sun}}\right|_{VL,PAC-EOL} \approx 2{,}32 \cdot 10^{-10}$$

4.4 Stray-light due to cosmetic defects

The contributor to stray-light due to scratches and digs S/D is analysed according to Ref.[13]. We assumed a worst case scenario of S/D 20/10 for mirrors cosmetics. The BSDF for the digs (diameter of the dig $d = 0{,}1mm$) and for the scratches (width w=0,02mm) are respectively given by (Ref. [10]):

$$BSDF_{digs} = \frac{N_d d^2}{4} \cdot \left[1 + \frac{\pi^2 d^2}{4\lambda^2}\left(1 + \frac{\sin^2\theta}{l_d^2}\right)^{-3/2}\right] \qquad BSDF_{scratches} = \frac{N_s w l}{\pi} \cdot \left[1 + \frac{\pi w l}{\lambda^2}\left(1 + \frac{\sin^2\theta}{l_s^2}\right)^{-3/2}\right]$$

where $N_d = \frac{1}{5\pi D}$ and $N_s = \frac{1}{\pi l D}$ are the densities of the digs and of the scratches, D is the diameter of the optics and $l = s_{max} D$. The roll-off angles are evaluated with the formulas $l_d = \left(\frac{4}{\pi^4}\right)^{1/3} \frac{\lambda}{d}$ and $l_s = \left(\frac{1}{2\pi^2}\right)^{2/3} \frac{\lambda}{(w^2 l)^{1/3}}$.

The evaluated BSDF functions for the scratches and the digs are summed and the resulting curve is fitted with an analytical ABg model for each optical element. The parameters A, B and g are applied to the optical surfaces of the model of the Telescope for a simulation dedicated to cosmetic defects only. The simulation is performed with 2E5 analysis rays.

Item	*D (mm)*	*Parameters of the ABg model*	*Wavelength (nm)*	*TIS*
Mirror M1	163	A = 7,2E-5, B = 1E-5, g = 1,5	633	0,0008873
Mirror M2	219	A = 7,2E-5, B = 1E-5, g = 1,5	633	0,0008873
window of the MCP	30	A = 1,1E-4, B = 1E-5, g = 1,5	633	0,0013463
Interferential Filter	80	A = 8,5E-5, B = 1E-5, g = 1,5	633	0,0010403
CD, BP, QWP, PMP	27	A = 1,65E-4, B = 1E-5, g = 1,5	633	0,0020194
LP, FLS	39	A = 1,1E-4, B = 1E-5, g = 1,5	633	0,0013463

Table 4-5. Parameters of the ABg model fitting the BSDF for a scratches and digs cosmetics of 20-10.

Figure 4-11 shows the modelled BSDF curves for the mirror M1 for roughness, cosmetics and particulate contamination.

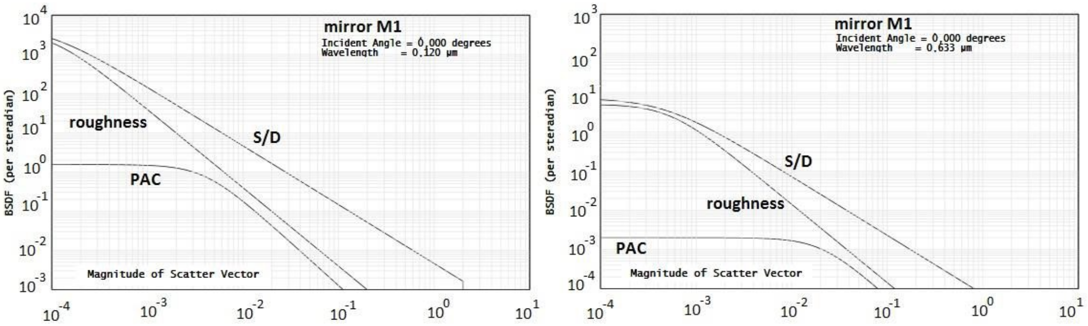

Figure 4-11. Modelled BSDF curves for mirror M1 at 121nm (left) and at 633nm (right).

The results of the simulation are in Table 4-6.

Item	*Averaged B_{stray} (Watt/cm^2) due to cosmetics*	*Averaged B_{corona} (Watt/cm^2)*	B_{stray}/B_{corona}
UVDA	2,31E-8 in [-4; 4]mm	4,71E-4	4,91E-5
VLDA	1,64E-7 in [-4; 4]mm	7,69E-3	2,12E-5

Table 4-6. Simulated irradiance and ratio B_{stray}/B_{corona} due to cosmetic defects.

The ratio B_{stray}/B_{corona} due to cosmetic defects, calculated as in Sect. 4.1.2, results $4{,}91 \cdot 10^{-4}$ for the UV channel and $2{,}12 \cdot 10^{-5}$ for the VL channel. Considering that the ratio of the corona to the disk irradiance is approximately $5 \cdot 10^{-5}$ at the HI-Lyman alpha (121,6nm) and approximately $1 \cdot 10^{-6}$ in the visible light (Ref.[7]) we obtain:

$$\left.\frac{\mathrm{B_{stray}}}{\mathrm{B_{sun}}}\right|_{UV,S-D} \approx 2{,}45 \cdot 10^{-9} \quad \text{and} \quad \left.\frac{B_{stray}}{B_{sun}}\right|_{VL,S-D} \approx 2{,}12 \cdot 10^{-11}$$

4.5 Results for the stray-light

The contributors to stray-light level due to surface micro-roughness, to diffraction, to particulate contamination and to cosmetics on the UV and VL focal planes are reported in Figure 4-12. The higher level of noise in the UV channel is due to the lower statistics (approximately a ratio 4:1) generated by the beam splitter coating of the IF. Figure 4-13 reports the stray-light level due to surface micro-roughness at the minimum perihelion and at 0,5AU.

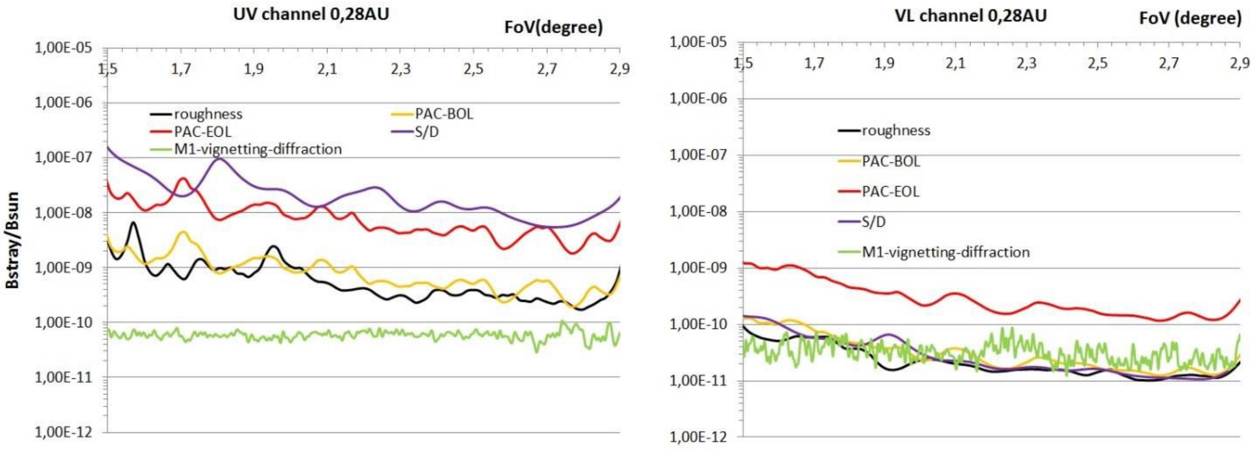

Figure 4-12. Contributors to stray-light level on the UV (left) and VL (right) focal planes.

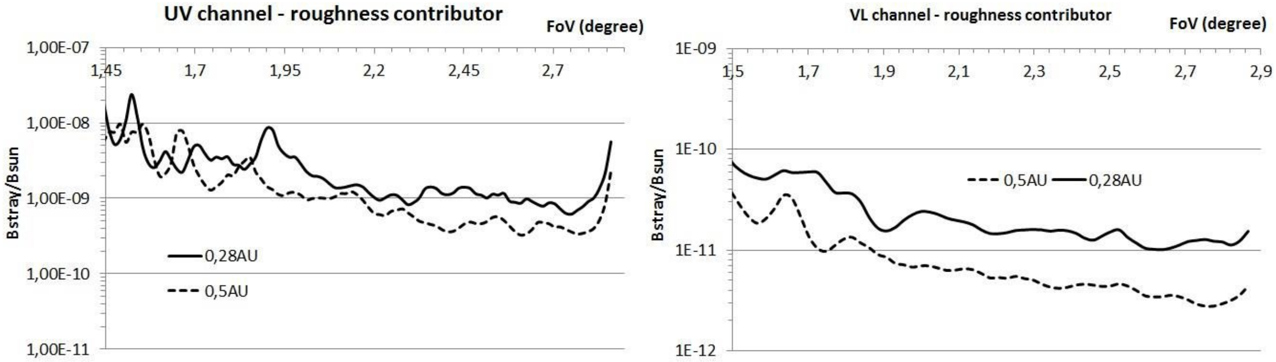

Figure 4-13. Roughness contributor to stray-light level on the UV (left) and VL (right) focal planes at 0,28AU and 0,5AU.

4.6 Comparison to the stray-light analysis with a semi-analytical model

A different type of stray-light analysis was carried out by numerically calculating the diffraction pattern on the M1 plane (Ref.[9]) for a wavelength of 600 nm, and then by propagating the obtained profile with the theory of scattering due to surface micro-roughness. The implemented BRDF model has a lorentzian profile (as described in Ref.[7]), with a roughness of 0.3 nm and a scattered beam semi-aperture of 1.97°. A level 300 (according to Mil-STD-1246) particle contamination has been implemented as well, by means of the BRDF provided in Ref.[14] and shown in Figure 4-14.

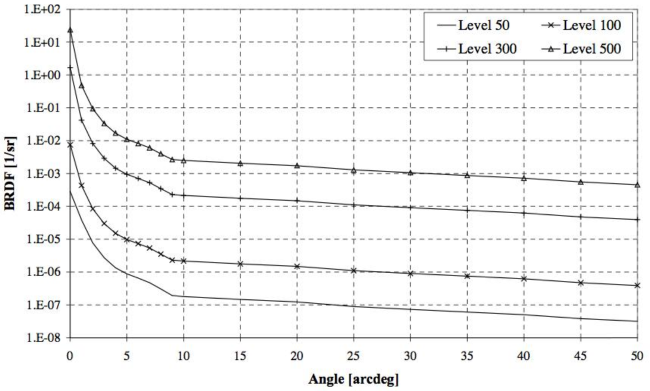

Figure 4-14 Effective BRDF for different levels of particle contamination levels according to Mil-STD-1246 (Ref.[14])

The calculation has been reproduced for a set of different heliocentric distances of METIS: the calculation has been run each time by setting the solar disk divergence at the values corresponding to the different heliocentric distances.
The plots in Figure 4-15 show the results obtained. They are consistent with the stray-light levels obtain with the previous analysis (Figure 4-12), considering the different approaches.

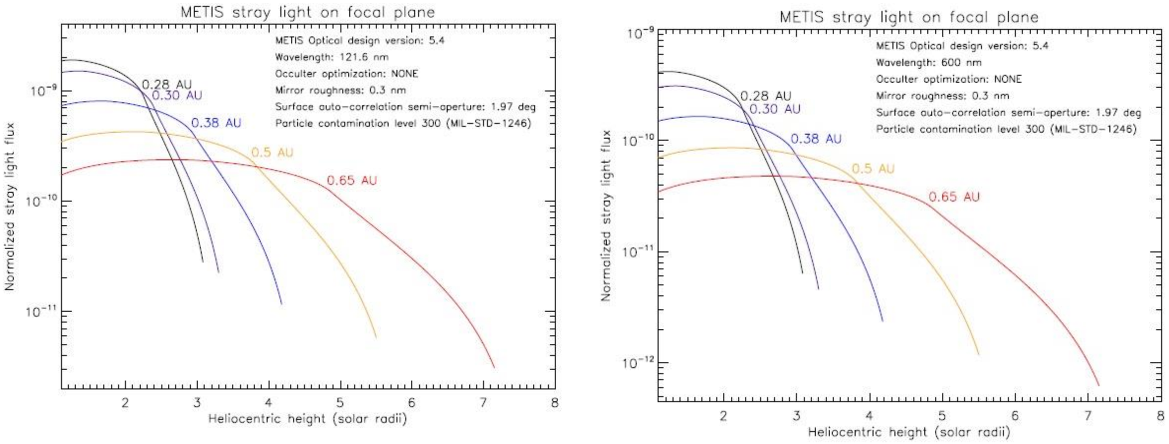

Figure 4-15. Estimated stray-light on the focal plane for different distances from the Sun. Normalized UV/VL flux (left/right).

4.7 Comparison to the stray-light analysis with ASAP

A preliminary ray tracing analysis has been previously carried out with Advanced Systems Analysis Program (ASAP ®) from Breault Research Organization, Inc. and it was already described in Ref.[3]. We report here some of the results obtained for a quick comparison with the above Zemax analysis.
We have implemented an opto-mechanical model of the coronagraph in which a Monte Carlo ray tracing analysis has been performed. The simulation considers an assigned roughness for the optomechanical surfaces hit and it generates a son ray by using the normalized bidirectional scattering distribution function as a probability distribution. The total energy reflected is brought by the single ray generated, with no loss of energy due to the rays sampling.
Also when a scattered ray hits a new surface, the code randomly generates a new ray, selected according to the distribution of the transmitted energy. The process can be stopped either after a certain value of scatter order or when the single ray has fallen below an energy threshold.
For the VL channel we considered λ= 600 nm as reference wavelength, and a square source in front of the entrance aperture composed by a grid of 5000 x 5000 rays, so that a beam composed by approximately 19 millions of rays enters the instrument. The rays are emitted within an angular aperture of 0.95°, that is, the angular radius of the Sun seen by METIS at the perihelion.
The UV channel considers a grid of 4600x4600 for a λ= 121.6 nm and the same angular aperture of the beam. In order to investigate the surface roughness of the used materials, we simulated three different micro-roughness for all the scattering surfaces for both UV and VL channels, with an average roughness R_a described as:

$$R_a = \frac{1}{L}\int_0^L |z(x)|\, dx$$

where L is the length of the sampling region on the material surface and $z(x)$ is a function which describes the surface one-dimensional profile.
In particular, three different values of R_a have been taken into account:

R1: $R_a = 0.1$ μm corresponding to a perfectly smooth surface obtained with lapping process
R2: $R_a = 1.0$ μm corresponding to an extra-fine grinding for machine tools
R3: $R_a = 3.0$ μm corresponding to a smooth grinding for machine tools

The roughness simulation assigns random gaussian distributed heights around the chosen parameter to the surface and assigns a certain variation of the surface orientation in micro zones of the surface itself. When a single ray hits a point on this surface, the response to the incoming light depends on the physical properties of the material under analysis. This study takes into account only one particular BSDF for the black coating of the mechanical elements (Figure 4-16). The panel returns the value of BSDF for some values of the incidence angle.

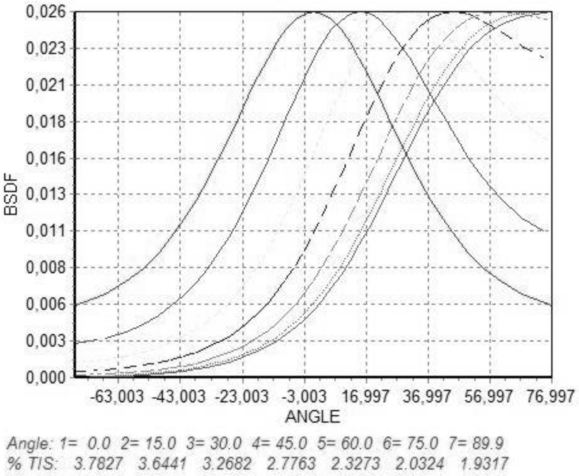

Figure 4-16. BSDF for the black coating considered for the mechanical elements for different incidence angles (in degrees).

All the optical elements have been simulated as polished mirrors having a surface roughness of λ/30, while the volume scattering due to the dioptric elements (glass imperfection etc.) has not been considered in this analysis, as well as the cosmetic defects and the particulate contamination.

If the simulated beam from the disk is composed by N rays, the total beam energy is B_{sun} and each single first generation ray carries an energy equal to 1/N of the total, that is, B/N. To reduce the calculation time we imposed two threshold values for the scattered rays: a limit of a 6th generation of scatter and a limit of 10^{-15} times in the energy carried by the single ray compared with the initial flux.

The number of rays surviving the multiple scatters multiplied by their intensities is integrated over the detectors surface and then compared with the number of rays of intensity 1 that would reach the detector if it were directly illuminated by the disk radiation (the stray light intensity is normalized to the disk emission intensity).

In the VL channel, the total flux integrated on the detector surface indicates it is slightly dependent on the surface roughness. Total flux of stray light on the detector in fraction of the photospheric flux entering the instrument for the VL channel is reported in the Table 4-7 and the straylight rays distribution on the detector is shown in Figure 4-17.

Average roughness considered R_a	B_{stray}/B_{sun}
R1: 0.1 μm	8.30E-12
R2: 1.0 μm	2.38E-11
R3: 3.0 μm	3.07E-11

Table 4-7. Total flux of stray light on the detector in units of the Sun-disk flux entering the instrument for the VL channel.

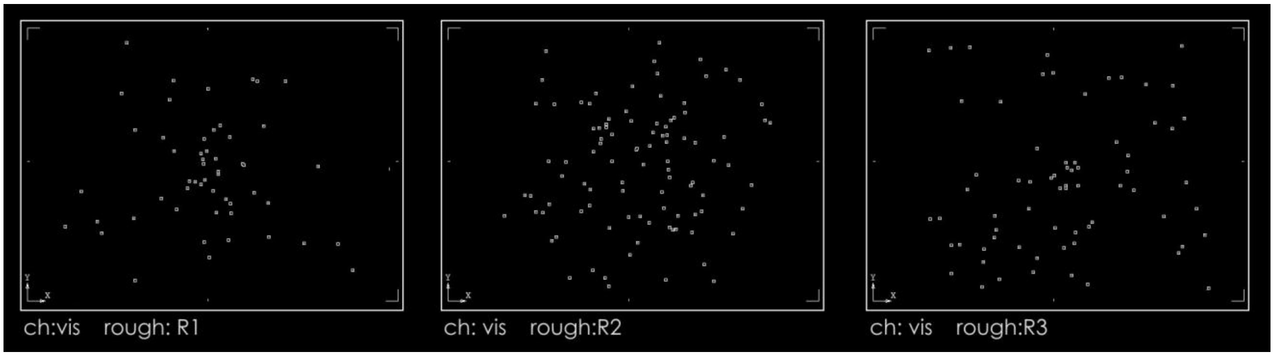

Figure 4-17. Straylight rays on the detector for the visible light path for the three roughness parameters considered.

The same analysis has been done for the UV 121.6 nm channel. Total flux of stray light on the detector in fraction of the photospheric flux entering the instrument for the UV channel in function of the three roughness parameters considered is reported in Table 4-8 and the straylight rays distribution on the detector is shown in Figure 4-18.

Average roughness considered R_a	$\mathrm{B_{stray}/B_{sun}}$
R1: 0.1 μm	8,06E-10
R2: 1.0 μm	8,82E-10
R3: 3.0 μm	9,25E-10

Table 4-8. Total flux of stray light on the detector in units of the Sun-disk flux entering the instrument for the UV channel.

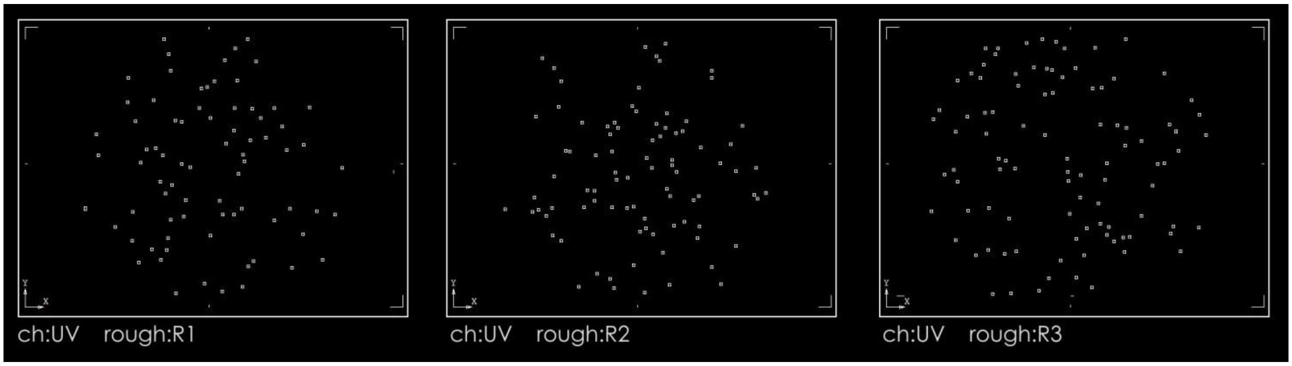

Figure 4-18. Straylight rays on the detector for the UV path for the three roughness parameters considered.

The results obtained with this analysis are in agreement with those shown in Figure 4-15 calculated with the Zemax code.

4.8 Conclusions

The results of all the analyses performed are summarized in Table 4-9.

Type of Analysis	$\mathrm{B_{stray}/B_{sun}}$ *(FOV=2°: at 0.28 AU)*				*References in this work*
	Particle contam. level 300		*No particle contamination*		
	Visible-light	*UV 122 nm*	*Visible-light*	*UV 122 nm*	
Montecarlo ray-trace (ASAP)	-	-	3.e-11	1.e-9	Table 4-7, 4-8
Semi-analytical (Ref.[7], [14])	3.e-10	2.e-9	-	-	Figure 4-15
Non-sequential ray-trace (Zemax)	~2.e-10	~9.e-9	~3.e-11	~2.e-9	Figure 4-12,[1] 4-13

Table 4-9 – Summary of the levels of stray-light resulting from all the types of analysis performed in this work

Considering that the three approaches were developed independently, the results are in considerable agreement and show compliance to the requirement of stray-light level for both the UV and VL channels.
The required ratios between the stray light irradiance B_{stray} (photons cm^{-2}s^{-1}) measured on the telescope focal plane to the solar disk mean irradiance B_{sun}, compared to those obtained from our analyses are:

- for the VL channel: $(\mathrm{B_{stray}/B_{sun}})_{VL\ analysis} < 3.\times 10^{-10} < (\mathrm{B_{stray}/B_{sun}})_{VL\ requirement} = 10^{-9}$;
- for the UV channel $(\mathrm{B_{stray}/B_{sun}})_{UV\ analysis} < 9.\times 10^{-9} < (\mathrm{B_{stray}/B_{sun}})_{UV\ requirement} = 10^{-7}$.

Even in the worst case of level-300 particle contamination at the end-of-life the estimated levels of stray light of METIS are an order of magnitude lower than the requirements.

---

[1] End-of-life

4.9 Acknowledgements

This work has been funded by ASI by industrial contract #2013-057-I.0 and by scientific contract #I/013/12/0.
The authors would like to thank Matteo Taccola of ESA and Denis Naughton of CGS for fruitful discussions in setting up the models.

5. REFERENCES

Ref.[1] S. Fineschi, E. Antonucci, G. Naletto, et al. *METIS: a novel coronograph design for the Solar Orbiter Mission*, Proc. Of SPIE Vol. 8443, (2012).

Ref.[2] E. Antonucci, S. Fineschi et al. *Multi element Telescope for imaging and spectroscopy (METIS)*, SPIE 8443-08 (2012).

Ref.[3] E. Verroi, V. Da Deppo, G. Naletto, S. Fineschi, E. Antonucci, *METIS-ESA Solar Orbiter Mission Internal Stray-Light Analysis*, ICSO (2014).

Ref.[4] Harvey-Shack and ABg BSDF in *Practical Optics Seminar*, Photon Engineering (2009).

Ref.[5] J.E. Harvey et al. *Total integrated scatter from surfaces with arbitrary roughness, correlation width and incident angles*, Optical Engineering 51(1), 013402 (January 2012).

Ref.[6] OpticStudio User Manual, page 1395 (May 2015).

Ref.[7] S. Fineschi, M. Romoli et al., *Stray Light Analysis of a Reflecting UV Coronagraph/Polarimeter with Multilayer Optics*, SPIE Vol. 2010 X-Ray and Ultraviolet Polarimetry (1993).

Ref.[8] M. Romoli et al. Stray-light suppression in a reflecting white-light coronograph, Applied Optics, vol. 32, 19 (1993).

Ref.[9] F. Landini et al. *Improved stray light suppression performance for the Solar Orbiter/METIS inverted external occulter*, Proc. of SPIE Vol. 8862 886204-1.

Ref.[10] P.R. Spyak, W.L. Wolfe; "*Scatter from particulate contaminated surfaces*", Appl. Opt. 31 (8) (1992).

Ref.[11] M. G. Dittman, *"Contamination scatter functions for stray-light analysis"*, Proceedings of SPIE Vol. 4774 (2002).

Ref.[12] Lallo, Matt, Petro, Larry, "*Bidirectional Reflectance Distribution Function for the NGST Mirrors*" Space Telescope Science Institute

Ref.[13] G. Peterson, *A BRDF model for scratches and digs* (SPIE 2012).

Ref.[14] J.Y. Plesseria et al., "Guidelines for contamination control of space optical systems", CSLTechnical Report UG.CSL.CLE.00001, (2001),